PHYSICAL REVIEW A **93**, 013805 (2016)

All-optical polarimetric generation of mixed-state single-photon geometric phases

D. Barberena, O. Ortíz, Y. Yugra, R. Caballero, and F. De Zela
Departamento de Ciencias, Sección Física, Pontificia Universidad Católica del Perú, Apartado 1761, Lima, Peru

(Received 14 October 2015; published 5 January 2016)

We report robust polarimetric measurements of mixed-state geometric phases. An all-optical setup was used to generate geometric phases with great versatility, thereby extending the scope of analogous methods used in neutron polarimetry. Our method allows us to explore geometric phases generated by unitarily evolving mixed states. These are realized as partially polarized single-photon states whose degree of polarization and normalized Stokes vector can be fixed independently of one another. The geometric phases correspond to both open and closed trajectories in Poincaré space. By exploiting the gauge invariance of geometric phases we nullify their dynamical part, thereby making the geometric phase coincide with the total (Pancharatnam) phase, which can be directly addressed by employing standard techniques.

DOI: 10.1103/PhysRevA.93.013805

I. INTRODUCTION

An important task of current interest consists of extending the concept of geometric phase to the case of mixed states [1–6]. The motivation comes mainly from the fact that mixed states are the ones we have to deal with in real life, especially when dealing with applications in quantum information. Two widely used definitions of geometric phases for mixed states are Uhlman's phase [7] and Sjöqvist's phase [8]. While the former was theoretically motivated, the latter has an operational meaning based on interferometry. Thus, it is nothing but natural that Sjöqvist's phase has been more extensively tested in experiments compared to Uhlman's phase. However, even though Sjöqvist's phase has been experimentally explored, the reported results do not exhibit all its predicted features, mainly because the paths followed by state vectors have been constrained to a limited class. The most versatile experiments have been carried out with polarized neutrons [9] and with nuclear magnetic resonance [10,11]. In the case of polarized neutrons, besides interferometry, polarimetric methods [12] have also been employed with some advantage. Polarimetry has, indeed, a natural robustness that derives from being based on a single-beam configuration. Mixed-state geometric phases generated with all-optical setups have not been extensively explored so far, even though they are very versatile for testing the robustness and viability of geometric gates and other quantum information applications. These are among the main reasons for exploring various features of geometric phases [13–15]. The present work addresses Sjöqvist's phase for mixed states by employing an all-optical polarimetric setup. We apply a recently demonstrated secondary source of partially polarized light [16] to generate polarization mixed states with great versatility. We have adapted this source to the case of single photons, thereby having a means to control the length and direction of the Stokes vector independently of one another. Previous single-photon experiments that were based on interferometric techniques have been constrained to explore closed trajectories made of geodesic paths on the Poincaré sphere and its interior [17]. Similarly, experiments using polarized neutrons [9] have exhibited geometric phases that were given in terms of the solid angle enclosed by a geodesic path and its shortest geodesic closure on the Bloch sphere. In this case, polarimetric techniques were employed to test mixed-state phases accumulated by neutrons being injected in states with different purities [9]. Such experiments are technologically very demanding, as they need a nuclear reactor as a source, pulsed magnetic fields to generate the required spin rotations, a ^{3}He neutron detector with high efficiency at an energy range that must be preselected with pyrolytic graphite crystals, polarizing and analyzing supermirrors, and so on [9]. In comparison, all-optical setups are considerably less demanding. In our setup, we exploit a recently demonstrated polarimetric technique to generate and test geometric phases associated with arbitrary paths on the Poincaré sphere [18]. This technique allows us to nullify the dynamical contribution to the total (Pancharatnam) phase [19], thereby making the latter coincide with the geometric phase. The gauge-invariant character of the geometric phase, i.e., its invariance under local phase changes $|\psi(s)\rangle \rightarrow |\psi'(s)\rangle = \exp[i\alpha(s)]|\psi(s)\rangle$, clearly shows up through this approach. Our experimental results are in very good agreement with theoretical predictions and serve as a proof of principle for polarimetric, all-optical techniques to generate geometric phases.

The rest of this paper is organized as follows. We first present in Sec. II the theoretical background of our polarimetric approach to the generation of mixed-state geometric phases. This comprises the general formula for these phases as well as the method we use to measure them by polarimetry. In Sec. III we describe our all-optical setup and present our experimental results. We close the paper with our conclusions.

II. POLARIMETRY

Interferometric techniques involving two beams can be mirrored by polarimetric, single-beam techniques. Instead of using a dichotomic path degree of freedom, on which interferometry is often based, one can use a dichotomic polarization degree of freedom. Let us consider, for example, a Mach-Zehnder interferometric array. If we assign the vectors $|\pm\rangle$ to the two paths of the interferometer, the total action of this device on an input state $|\psi\rangle \in \mathrm{Span}\{|+\rangle,|-\rangle\}$ is given by $|\psi\rangle \rightarrow U_{\mathrm{BS}} U_{\varphi} U_{\mathrm{BS}} |\psi\rangle$, where $U_{\mathrm{BS}} = (\sigma_x + \sigma_z)/\sqrt{2}$ and $U_{\varphi} = \exp(i\varphi\sigma_z/2)$ represent the individual actions of the beam splitter and phase shifter, respectively [20]. Here, $\sigma_{i=x,y,z}$ are the standard Pauli matrices. The intensity that is recorded at the outputs $|\pm\rangle$ is then given by $I_\pm = |\langle\pm|U_{\mathrm{BS}}U_\varphi U_{\mathrm{BS}}|\pm\rangle|^2 = (1 \pm \cos\varphi)/2$. If we now assume that $|\pm\rangle$ no longer correspond to path but to polarization states, interferometry turns into polarimetry. In such a case, U_φ and U_{BS} can be implemented with quarter-wave plates Q and half-wave plates H as $U_\varphi = Q(\pi/4)H[(-\varphi - \pi)/4]Q(\pi/4)$ and $U_{\mathrm{BS}} = iH(\pi/8)$. The arguments in H and Q refer to the angles made by the plate's major axis and the vertical direction. Up to a global phase factor (of $e^{i\pi}$), the transformation $U_{\mathrm{BS}}U_\varphi U_{\mathrm{BS}}$ in polarization space can be brought to the form $Q(\pi/2)H[(2\pi - \varphi)/4]Q(\pi/2)$. A detector with a polarizer before it lets us record the intensity as a function of φ, thereby getting a pattern that is equivalent to the interferogram produced by the Mach-Zehnder array. Polarimetry is largely insensitive to thermal and mechanical perturbations that produce random phase shifts in the case of interferometry. However, because the states $|\pm\rangle$ cannot be individually addressed, as is the case with interferometry, we must figure out how to go around this constraint in order to extract the desired information. In the case of geometric phases this is indeed possible, as we show below. But before that and for the sake of completeness, we give a short account of mixed-state geometric phases, the main subject matter of this work.

A. Mixed-state geometric phases

According to the kinematic approach [21], the geometric phase is given by

$$\Phi_g(\mathcal{C}) = \arg\langle\psi(0)|\psi(s)\rangle - \mathrm{Im}\int_0^s \langle\psi(s')|\dot{\psi}(s')\rangle ds' \tag{1}$$

for a path $\mathcal{C}$ joining the initial state $|\psi(0)\rangle$ with the final state $|\psi(s)\rangle$, no matter which dynamics governs the evolution of the pure state $|\psi(s')\rangle$, as long as this evolution can be described as a path $\mathcal{C} : s' \in [0,s] \to |\psi(s')\rangle$. In (1), $|\dot{\psi}(s')\rangle$ stands for $d\,|\psi(s')\rangle\,/ds'$. The geometric phase contains a total (Pancharatnam) phase $\arg\langle\psi(0)|\psi(s)\rangle$ and a dynamic phase $\mathrm{Im}\int_0^s \langle\psi(s')|\dot{\psi}(s')\rangle ds'$. The sum of these two contributions makes Φ_g invariant under local gauge transformations $|\psi(s)\rangle \to |\psi'(s)\rangle = \exp[i\alpha(s)]|\psi(s)\rangle$. We can use this property to nullify either of the two contributions. In order to nullify the dynamic phase, we can gauge transform $|\psi(s)\rangle \to |\psi'(s)\rangle$ so that $\langle\psi'(s)|\dot{\psi}'(s)\rangle = 0$.

We can similarly address the evolution of mixed states $\rho(s)$ by considering the path $\mathcal{P} : s' \in [0,s] \to \rho(s') = \sum_k p_k(s')|\psi_k(s')\rangle\langle\psi_k(s')|$. Here, $p_k(s')$ are parameter-dependent occupation probabilities of the states $|\psi_k(s')\rangle$. The total (Pancharatnam) phase is given in this case by

$$\alpha(s) = \arg\left(\sum_{k=1}^{N}\sqrt{p_k(0)p_k(s)}\langle\psi_k(0)|\psi_k(s)\rangle\right). \tag{2}$$

The two orthonormal bases, $\{|\psi_k(0)\rangle\}$ and $\{|\psi_k(s)\rangle\}$, are related to each other by some unitary transformation $U(s)$, such that $|\psi_k(s)\rangle = U(s)|\psi_k(0)\rangle$. This transformation is not uniquely defined but belongs to a family whose members realize the given path $\mathcal{P}$. In order to define a geometric phase associated with $\mathcal{P}$, we may choose a unitary $U_\parallel$ that satisfies the parallel transport conditions $\langle\psi_k(0)|U_\parallel^\dagger(s)\dot{U}_\parallel(s)|\psi_k(0)\rangle = 0\ \forall\ k$. In such a case, the geometric phase for path $\mathcal{P}$ is given by

$$\Phi_g(\mathcal{P}) = \arg\left(\sum_{k=1}^{N}\sqrt{p_k(0)p_k(s)}\langle\psi_k(0)|U_\parallel(s)|\psi_k(0)\rangle\right). \tag{3}$$

The required $U_\parallel$ can be obtained from any unitary $U(s)$ such that $|\psi_k(s)\rangle = U(s)|\psi_k(0)\rangle$ by setting

$$U_\parallel(s) = U(s)\sum_{k=1}^{N} e^{-\int_0^s\langle\psi_k(0)|U^\dagger(s')\dot{U}(s')|\psi_k(0)\rangle ds'}|\psi_k(0)\rangle\langle\psi_k(0)|. \tag{4}$$

This leads to a geometric phase given by

$$\Phi_g(\mathcal{P}) = \arg\left(\sum_{k=1}^{N}\sqrt{p_k(0)p_k(s)}\langle\psi_k(0)|\psi_k(s)\rangle e^{-\int_0^s\langle\psi_k(s)|\dot{\psi}_k(s)\rangle ds'}\right). \tag{5}$$

The definition of $\Phi_g(\mathcal{P})$ does not restrict the evolution $\mathcal{P} : s' \in [0,s] \to \rho(s')$ to be generated by a unitary transformation $\rho(0) \to \rho(s) = U(s)\rho(0)$. Indeed, $\Phi_g(\mathcal{P})$ applies for unitary and nonunitary evolutions. When the evolution is unitary, p_k are parameter independent, and $\Phi_g(\mathcal{P})$ reads

$$\Phi_g(\mathcal{P}) = \arg\left(\sum_{k=1}^{N} p_k\langle\psi_k(0)|U(s)|\psi_k(0)\rangle \times e^{-\int_0^s\langle\psi_k(0)|U^\dagger(s')\dot{U}(s')|\psi_k(0)\rangle ds'}\right). \tag{6}$$

This is the case we address here, with $N = 2$ and $U(\alpha) = \exp[-i\alpha\mathbf{q}(\theta,\phi)\cdot\boldsymbol{\sigma}]$, where we have set $s = \alpha$ to emphasize that it denotes an angle. By applying $U(\alpha)$ to a polarization state $|\psi_k(0)\rangle$, the corresponding Stokes vector gets rotated an angle 2α around the unit vector $\mathbf{q} = (\sin\theta\cos\phi, \sin\theta\sin\phi, \cos\theta)$. In this case,

$$\int_0^\alpha \langle\psi_k(0)|U^\dagger(\alpha')\dot{U}(\alpha')|\psi_k(0)\rangle d\alpha' = -i\alpha\langle\psi_k(0)|\mathbf{q}\cdot\boldsymbol{\sigma}|\psi_k(0)\rangle. \tag{7}$$

B. Partially polarized single-photon states

The mixed states we use are partially polarized states. The general form of these states is given by

$$\rho = \tfrac{1}{2}(\mathbb{1} + r\mathbf{n}\cdot\boldsymbol{\sigma}), \tag{8}$$

with $r \in [0,1]$ denoting the degree of polarization and $\mathbf{n}$ being a unit vector. Thus, $r\mathbf{n}$ is the Stokes vector, whose length varies between 0 and 1. In terms of the eigenvectors $|\mathbf{n}_\pm\rangle$ of $\mathbf{n}\cdot\boldsymbol{\sigma}$, i.e., of ρ, we can write

$$\rho = \frac{1+r}{2}|\mathbf{n}_+\rangle\langle\mathbf{n}_+| + \frac{1-r}{2}|\mathbf{n}_-\rangle\langle\mathbf{n}_-|. \tag{9}$$

The vectors entering Eq. (7) are $|\psi_{k=\pm}(0)\rangle = |\mathbf{n}_\pm\rangle$ in the present case, for which we have

$$\langle\mathbf{n}_\pm|\mathbf{q}\cdot\boldsymbol{\sigma}|\mathbf{n}_\pm\rangle = \pm\mathbf{n}\cdot\mathbf{q} = \pm\cos\theta, \tag{10}$$

where θ is the angle between $\mathbf{q}$ and $\mathbf{n}$. As for $U_{\parallel}$ [see Eq. (4)], it is given by

$$U_{\parallel}(\alpha) = \exp(-i\alpha\mathbf{q}\cdot\boldsymbol{\sigma})[e^{i\alpha\cos\theta}|\mathbf{n}_+\rangle\langle\mathbf{n}_+| + e^{-i\alpha\cos\theta}|\mathbf{n}_-\rangle\langle\mathbf{n}_-|]. \tag{11}$$

The unit vector $\mathbf{q}$ is still expressed as $\mathbf{q} = (\sin\theta\cos\phi, \sin\theta\sin\phi, \cos\theta)$, where we take as the reference frame one whose triad of orthonormal unit vectors is given by $\mathbf{n}$, $\mathbf{m}$, and $\mathbf{n}\times\mathbf{m}$. That is, ϕ is the (azimuthal) angle between $\mathbf{m}$ and the projection of $\mathbf{q}$ on the plane whose normal is $\mathbf{n} = (0,0,1)$. In a matrix representation with $|\mathbf{n}_+\rangle = (1,0)^T$ and $|\mathbf{n}_-\rangle = (0,1)^T$, we have

$$\mathbf{q}\cdot\boldsymbol{\sigma} = \begin{pmatrix} \cos\theta & e^{-i\phi}\sin\theta \\ e^{i\phi}\sin\theta & -\cos\theta \end{pmatrix}. \tag{12}$$

The input state ρ is submitted to the transformation $U_{\mathrm{MZ}} = U_{\mathrm{BS}}U_{\parallel}(\alpha)U_{\varphi}U_{\mathrm{BS}}$ before being detected. In matrix form, U_{MZ} reads

$$U_{\mathrm{MZ}} = \begin{pmatrix} \cos\alpha\cos\chi + \sin\alpha[\cos\theta\sin\chi - i\cos(\phi+\chi)\sin\theta] & i(\cos\alpha\sin\chi - \cos\theta\cos\chi\sin\alpha) + \sin\alpha\sin\theta\sin(\phi+\chi) \\ i(\cos\alpha\sin\chi - \cos\theta\cos\chi\sin\alpha) - \sin\alpha\sin\theta\sin(\phi+\chi) & \cos\alpha\cos\chi + \sin\alpha[\cos\theta\sin\chi + i\cos(\phi+\chi)\sin\theta] \end{pmatrix}, \tag{13}$$

with $\chi = \varphi/2 + \alpha\cos\theta$.

The intensity that is recorded at the $|\mathbf{n}_+\rangle$-output channel is given by $I = \mathrm{Tr}\,(|\mathbf{n}_+\rangle\langle\mathbf{n}_+|U_{\mathrm{MZ}}\rho U_{\mathrm{MZ}}^{\dagger})$; explicitly,

$$I = \frac{1}{2} + \frac{r}{2}[\cos^2\alpha\cos 2\chi - \sin^2\alpha\cos^2\theta\cos 2\chi + \sin 2\alpha\cos\theta\sin 2\chi + \sin^2\alpha\sin^2\theta\cos(2\chi + 2\phi)]. \tag{14}$$

The geometric phase can be calculated from $\Phi_g = \arg\Phi_g^f$, where

$$\Phi_g^f = \frac{1+r}{2}\langle\mathbf{n}_+|U(\alpha)|\mathbf{n}_+\rangle e^{i\alpha\cos\theta} + \frac{1-r}{2}\langle\mathbf{n}_-|U(\alpha)|\mathbf{n}_-\rangle e^{-i\alpha\cos\theta}. \tag{15}$$

We readily obtain

$$\Phi_g = -\arctan\left(r\frac{\cos\theta\tan\alpha - \tan(\alpha\cos\theta)}{1 + \cos\theta\tan\alpha\tan(\alpha\cos\theta)}\right). \tag{16}$$

As for the Pancharatnam phase, it is given by

$$\Phi_P = -\arctan(r\cos\theta\tan\alpha). \tag{17}$$

We recover Φ_P from Φ_g by setting to zero in Eqs. (15) and (16) the additional phase shift $\alpha\cos\theta$ that was required to satisfy the parallel transport conditions, i.e., to nullify the dynamical contributions to Φ_g. Notice also that in the case of a closed trajectory ($\alpha = \pi$), Eq. (16) reduces to the experimentally tested [9,10,17] result

$$\Phi_g^c = -\arctan\left(r\tan\frac{\Omega}{2}\right), \tag{18}$$

with $\Omega = 2\pi(1-\cos\theta)$ being the solid angle enclosed by the trajectory on the Bloch sphere.

Equation (14) can be written in the form

$$I = \frac{1}{2} + \frac{r}{2}(X\cos 2\chi + Y\sin 2\chi), \tag{19}$$

with

$$X = \cos 2\alpha + 2\sin^2\alpha\sin^2\theta\cos^2\phi, \tag{20}$$

$$Y = \cos\theta\sin 2\alpha - \sin^2\alpha\sin^2\theta\sin 2\phi. \tag{21}$$

The extremal values of I are reached for $\chi = \chi_0$ such that $\cos 2\chi_0 = \pm X(X^2+Y^2)^{-1/2}$ and $\sin 2\chi_0 = \pm Y(X^2+Y^2)^{-1/2}$. They read

$$I_{\max} = \frac{1}{2} + \frac{r}{2}(X^2+Y^2)^{1/2}, \tag{22}$$

$$I_{\min} = \frac{1}{2} - \frac{r}{2}(X^2+Y^2)^{1/2}. \tag{23}$$

In principle, by relating X and Y with experimentally observable quantities such as $I_{\min}$, $I_{\max}$, and the visibility $V = r(X^2+Y^2)^{1/2}/2$, we can fix θ and α, which in turn determine Φ_g [see Eq. (16)]. However, for technical reasons, it is easier to implement the generation and measurement of Φ_g with an array that does not correspond exactly to the conceptually simplest one given by $U_{\mathrm{MZ}} = U_{\mathrm{BS}}U_{\parallel}(\alpha)U_{\varphi}U_{\mathrm{BS}}$ but slightly differs from it. Indeed, by using $U'_{\mathrm{MZ}} = U_{\mathrm{BS}}U_{\varphi}^{\dagger}U_{\parallel}(\alpha)U_{\varphi}U_{\mathrm{BS}}$ one has some experimental advantages, for instance, a constant intensity for $\alpha = 0$, which is useful for calibration purposes. Besides, it is difficult to determine parameters such as ϕ, which enter Eqs. (22) and (23). In contrast, ϕ' enters the intensity I given by Eq. (29) (see below) in such a way that $I_{\max}$ and $I_{\min}$ turn out to be independent of ϕ'. In order to use U'_{MZ} one has to redefine θ and α so that Φ_g is directly given by an expression that is identical to Eq. (17) but written in terms of the redefined θ and α. We describe next how this adaptation can be carried out.

C. Polarimetric array

The transformation $U_{\parallel}$ [see Eq. (11)] required to fulfil the parallel transport conditions belongs to the group SU(2), and as such it can be written in the form $U_{\parallel} = \exp(-i\alpha'\mathbf{q}'\cdot\boldsymbol{\sigma})$, with suitably defined α' and $\mathbf{q}'(\theta',\phi')$. Written in terms of these parameters, $\Phi_g = \Phi_P$ reads as given by Eq. (17). This is the expression against which we want to test our experimental results. As $U_{\parallel} \in \mathrm{SU}(2)$, it can be implemented with the help of three retarders, whose orientations can be numerically calculated and used to automatize data recording.

In order to put $U_{\parallel}$ in the desired form, it is convenient to proceed as follows. We write $U_{\parallel} = U_{\alpha}U_{\beta}$, with $U_{\alpha} = \exp(-i\alpha\mathbf{q}\cdot\boldsymbol{\sigma})$ and $U_{\beta} = e^{i\beta}|\mathbf{n}_+\rangle\langle\mathbf{n}_+| + e^{-i\beta}|\mathbf{n}_-\rangle\langle\mathbf{n}_-|$, where $\beta = \alpha\cos\theta$. Both U_{α} and U_{β} can be written in the form

$\cos\gamma - i\sin\gamma\mathbf{m}\cdot\boldsymbol{\sigma}$. This last expression can, in turn, be written in terms of two unit vectors, $\mathbf{n}_1$ and $\mathbf{n}_2$, as

$$A(\mathbf{n}_1,\mathbf{n}_2) := \mathbf{n}_1\cdot\mathbf{n}_2 - i\mathbf{n}_1\times\mathbf{n}_2\cdot\boldsymbol{\sigma}, \tag{24}$$

with $\mathbf{n}_1\cdot\mathbf{n}_2 = \cos\gamma$ and $\mathbf{n}_1\times\mathbf{n}_2 = \sin\gamma\mathbf{m}$. The quantity $A(\mathbf{n}_1,\mathbf{n}_2)$ is known as a "Hamilton turn" [22]. It can be graphically represented as a directed great circle arc going from $\mathbf{n}_1$ to $\mathbf{n}_2$ on the unit sphere. A straightforward calculation shows that $A(\mathbf{n}_2,\mathbf{n}_3)A(\mathbf{n}_1,\mathbf{n}_2) = A(\mathbf{n}_1,\mathbf{n}_3)$; that is, "turns" satisfy the same sum rule that holds for planar vectors but applied to directed arcs on the sphere. Just as a planar vector can be represented by any arrow in a family of equally oriented, parallel arrows, a turn can be represented by all directed arcs that can be obtained by sliding a given one along its great circle. This means that the unit vectors entering $A(\mathbf{n}_1,\mathbf{n}_2)$ are not uniquely defined. We can exploit this nonuniqueness in order to write $U_\parallel = U_\alpha U_\beta$ in the desired form. To this end, we express U_α and U_β such that they share a common vector $\mathbf{n}_2$:

$$\begin{aligned} U_\beta &= \mathbf{n}_1\cdot\mathbf{n}_2 - i\mathbf{n}_1\times\mathbf{n}_2\cdot\boldsymbol{\sigma}, \\ U_\alpha &= \mathbf{n}_2\cdot\mathbf{n}_3 - i\mathbf{n}_2\times\mathbf{n}_3\cdot\boldsymbol{\sigma}, \end{aligned} \tag{25}$$

with

$$\begin{aligned} \mathbf{n}_1 &= [-\sin(\alpha\cos\theta+\phi),\cos(\alpha\cos\theta+\phi),0], \\ \mathbf{n}_2 &= (-\sin\phi,\cos\phi,0), \\ \mathbf{n}_3 &= (-\cos\theta\cos\phi\sin\alpha - \cos\alpha\sin\phi,\cos\alpha\cos\phi \\ &\quad - \cos\theta\sin\phi\sin\alpha,\sin\alpha\sin\theta). \end{aligned} \tag{26}$$

This lets us bring $U_\parallel$ to the form

$$U_\parallel = \exp(-i\alpha'\mathbf{q}'\cdot\boldsymbol{\sigma}) = \cos\alpha' - i\sin\alpha'\mathbf{q}'\cdot\boldsymbol{\sigma}, \tag{27}$$

with $\cos\alpha' = \mathbf{n}_1\cdot\mathbf{n}_3$ and $\mathbf{q}'(\theta',\phi') = \mathbf{n}_1\times\mathbf{n}_3/\sqrt{1-(\mathbf{n}_1\cdot\mathbf{n}_3)^2}$. In this way we are provided with explicit expressions for α' and $\mathbf{q}'$ in terms of the input data. Next, we can express $\Phi_g = \Phi_P$ as in Eq. (17) with $(\alpha,\theta)\to(\alpha',\theta')$:

$$\Phi_g = -\arctan(r\cos\theta'\tan\alpha'). \tag{28}$$

Noting that $\cos\theta' = q_3'$, we get $\cos\theta'\tan\alpha' = (\mathbf{n}_1\times\mathbf{n}_3)_3/\cos\alpha' = (\mathbf{n}_1\times\mathbf{n}_3)_3/(\mathbf{n}_1\cdot\mathbf{n}_3)$. Calculating this last expression with the help of Eqs. (26) and inserting it into Eq. (28), we recover Eq. (16).

The intensity that corresponds to our present approach, i.e., $I = \mathrm{Tr}[|\mathbf{n}_+\rangle\langle\mathbf{n}_+|U'_{\mathrm{MZ}}\rho(U'_{\mathrm{MZ}})^\dagger]$, with $U'_{\mathrm{MZ}} = U_{\mathrm{BS}}U_\varphi^\dagger U_\parallel(\alpha)U_\varphi U_{\mathrm{BS}}$, is given by

$$\begin{aligned} I = {}& \frac{1+r}{2}\cos^2\alpha' + \frac{1-r\cos^2\theta'}{2}\sin^2\alpha' \\ &+ \frac{r}{2}\sin^2\alpha'\sin^2\theta'\cos(2\phi'-2\varphi). \end{aligned} \tag{29}$$

By calculating the minimum and maximum of I as a function of φ, we can express the geometric phase in terms of measurable quantities as

$$\Phi_g = -\arctan\left(r\sqrt{\frac{1+r-2I_{\max}}{2I_{\min}-1+r}}\right), \quad \alpha' < \pi/2, \tag{30}$$

$$\Phi_g = \arctan\left(r\sqrt{\frac{1+r-2I_{\max}}{2I_{\min}-1+r}}\right) - \pi, \quad \pi/2 < \alpha' < \pi. \tag{31}$$

These are the theoretical expressions that we have submitted to experimental test. They correspond to trajectories in Poincaré space that can be open or closed. Although we have focused on circular trajectories, our approach applies for a great variety of paths, which becomes clear by looking at the technical details of our array, which we address next.

III. EXPERIMENTAL SETUP AND RESULTS

Our experimental array is shown in Fig. 1. Its main parts are a preparation stage where the mixed states can be produced, followed by a second stage where the geometric phase is generated and a third stage for counting probabilities in coincidence with heralding photons.

In each run, two photon beams (800 nm) are produced in a beta barium borate (BBO) crystal by type-I spontaneous parametric down-conversion. The BBO crystal is pumped by a cw diode laser (measured central wavelength of 400 nm, spectral linewidth between 0.5 and 1 nm, and output power of 37.5 mW). The heralding photon beam is directed towards an avalanche photodetector, while the signal beam is directed towards the preparation stage. Coincidence counts of heralding and signal beams are defined within a time window of 10.42 ns. Our photon-counting module (Perkin-Elmer SPCM-AQ4C) has a dark count rate of 500 ± 10 counts/s. Photons are collected with the help of converging lenses that focus them into multimode fiber-optic cables with fiber-coupling connectors at both ends. In front of our detectors we set dichroic filters (Thorlabs FB800-40, FWHM: 40 ± 8 nm) that are centered at 800 ± 8 nm. Single-photon production is checked by measuring the degree of second-order coherence $g^{(2)}$ between the reflected (R) and transmitted (T) beams of a beam splitter [23,24]. Detections at gates T and R are conditioned upon detection at a third gate, G. In that case,

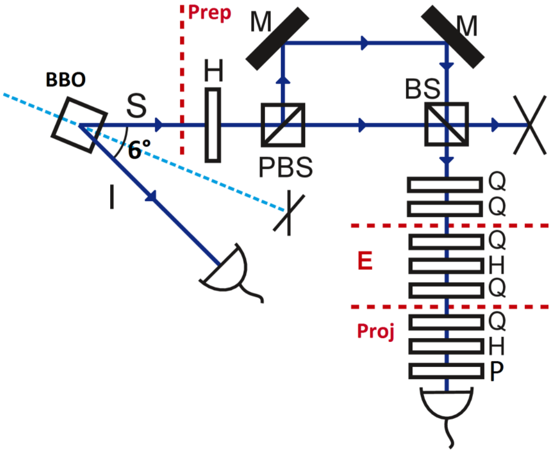

FIG. 1. Experimental setup. In the preparation stage (Prep) the degree of polarization of single photons, generated by parametric down-conversion, is fixed by incoherently mixing $|H\rangle$ and $|V\rangle$ polarization states, after which the Stokes vector is brought to its desired orientation with the help of two quarter-wave plates. The next stage (E) consists of a QHQ array that implements the required unitary transformation (see text). The projection stage (Proj) serves to normalize coincidence counts (in the $|\mathbf{n}_\pm\rangle$ basis) between idler (I) and signal (S) photons.

$g^{(2)} = P_{\mathrm{GTR}}/(P_{\mathrm{GT}}P_{\mathrm{GR}})$, where P_k denote probabilities for simultaneous detection at gates specified by label k. In terms of photocounts N_k, the degree of coherence can be expressed as $g^{(2)} = N_{\mathrm{GTR}}N_G/(N_{\mathrm{GT}}N_{\mathrm{GR}})$ [25]. A value $g^{(2)} < 1$ corresponds to nonclassical light. In our case, $g^{(2)} = 0.187 \pm 0.011$.

Our preparation stage consists of two substages, one for fixing the degree of polarization r followed by a second part that serves to fix the orientation of the Stokes vector. In the first substage the horizontally polarized state $|H\rangle$ of an input photon is transformed to $\cos\theta_r|H\rangle + \sin\theta_r|V\rangle$. This pure state is submitted to the action of a polarizing beam splitter (PBS) followed by two polarizers, one on each output arm of the PBS. One polarizer is set to 0° and the other to 90° to ensure that both beams are either parallel or plane polarized with respect to the reflection surface of a second beam splitter (BS), thereby preventing the appearance of spurious phase shifts. The pure state $\cos\theta_r|H\rangle + \sin\theta_r|V\rangle$ comes out from the second BS as the mixed state $\cos^2\theta_r|H\rangle\langle H| + \sin^2\theta_r|V\rangle\langle V|$. This occurs because the difference in arm lengths is larger than the photon coherence length, which is on the order of 10 μm. The angle θ_r is set so that $\cos^2\theta_r = (1+r)/2$. The mixed state exiting the second beam splitter is subsequently converted to the desired state, $\cos^2\theta_r|\mathbf{n}_+\rangle\langle\mathbf{n}_+| + \sin^2\theta_r|\mathbf{n}_-\rangle\langle\mathbf{n}_-|$, with the help of two quarter-wave plates, which perform the transformation $\{|H\rangle\langle H|, |V\rangle\langle V|\} \to \{|\mathbf{n}_+\rangle\langle\mathbf{n}_+|, |\mathbf{n}_-\rangle\langle\mathbf{n}_-|\}$. In this way, polarization states given by $\rho = (\mathbb{1} + r\mathbf{n}\cdot\boldsymbol{\sigma})/2$ can be prepared and launched to the next stage, where they are submitted to unitary evolution along the targeted paths in Poincaré space. As already explained, the unitary evolution must be supplemented by an additional one that serves the purpose of nullifying the dynamical contribution to the geometric phase. We must also generate the U_{BS} and U_φ transformations in order to simulate the Mach-Zender interferometer. The complete unitary transformation is $U_{\mathrm{BS}}U_\varphi^\dagger U_\parallel(\alpha)U_\varphi U_{\mathrm{BS}}$. In order to address separately the evolutions generated by U_{BS}, U_φ, and $U_\parallel$, respectively, we would need 18 retarders. However, this is unnecessary in the present case. Our full unitary transformation can be implemented with just three retarders in the configuration QHQ (see Fig. 1), stage E. Besides the unitary transformation it is also necessary to characterize the states for which a QHP array has been used, where P stands for polarizer.

Once the initial state and the evolution have been chosen, the geometric phase can be generally determined by the following measuring procedure: a point in the evolution curve is selected [by fixing α in $U(\alpha)$], and then an interferogram is generated by varying φ [see Eq. (29)]. In principle, we would only need to vary the settings in the E stage (see Fig. 1), but it proves useful to measure the orthogonal projections as well, in order to normalize the counts of coincidences. The geometric phase can then be fixed by first finding maximal and minimal intensities of the interferogram (either by fitting it to a suitably parametrized sinusoidal curve or by Fourier inversion), after which one needs only to introduce these extremal values in Eq. (30) or Eq. (31), so as to obtain a continuous curve as α varies. The values of the measured geometric phases should coincide, within experimental uncertainties, with the theoretical ones that are obtained by using Eq. (16). As Fig. 2 shows, this is indeed the case. We should stress that the solid curves shown in Fig. 2 are not fits to the measured values but theoretical predictions without adjustable parameters.

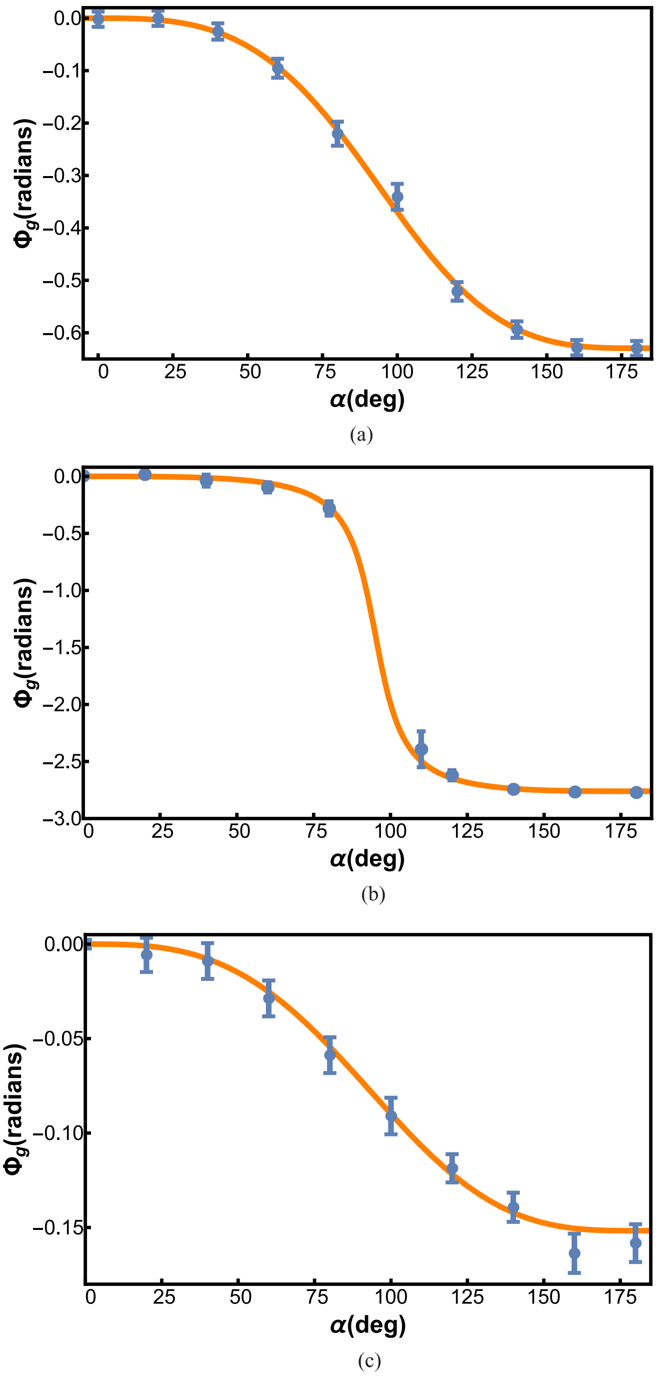

FIG. 2. Geometric phases as a function of the evolution parameter α for three different initial mixed states and evolutions. The experimentally measured values (dots) are shown with their error bars. They closely agree with theoretical predictions (solid curves). The curves correspond to the evolutions shown in Fig. 3. (a) Initial state: $r = 0.7 \pm 0.01$, $\hat{n} = (0.31 \pm 0.05, 0.59 \pm 0.05, 0.75 \pm 0.04)$. Axis of rotation: $\hat{q} = (0,1,1)$. (b) Initial state: $r = 0.4 \pm 0.01, \hat{n} = (0.71 \pm 0.03, 0.5 \pm 0.04, 0.5 \pm 0.04)$. Axis of rotation: $\hat{q} = (0.85, -0.45, -0.26)$. (c) Initial state: $r = 0.3 \pm 0.01, \hat{n} = (0.71 \pm 0.03, 0.5 \pm 0.04, 0.5 \pm 0.04)$. Axis of rotation: $\hat{q} = (0.31, 0.4, 0.86)$.

Depending on the case at hand, the general measuring procedure must be refined in order to achieve the desired accuracy. There are also cases in which the geometric phase is too sensitive to experimental inaccuracies and no reliable results can be found. Figure 2 shows three illustrative examples of data recording. As explained below, in each of these cases it was required to apply some slight modification of the general measuring procedure in order to achieve the desired accuracy. These examples show that our experimental results fit very well theoretical predictions, i.e., that our array produces the prescribed mixed-state geometric phases. Each curve shows the geometric phase acquired by an initial state that traverses a circular trajectory in Poincaré space (see Fig. 3). Since the associated evolutions are unitary, each trajectory is contained in a sphere whose radius is fixed by the purity of the state. The geometric phases in Fig. 2 correspond to initial states with degrees of polarization $r = 0.7 \pm 0.01$, 0.4 ± 0.01, and 0.3 ± 0.01 and with normalized Stokes vectors given by $(0.31 \pm 0.05, 0.59 \pm 0.05, 0.75 \pm 0.04)$ in the first case and by $(0.71 \pm 0.03, 0.5 \pm 0.04, 0.5 \pm 0.04)$ in the second and third cases. The states perform rotations around three different axes $\hat{q}$, nominally given by $(0,0,1)$, $(0.85, -0.45, -0.26)$, and $(0.31, 0.4, 0.86)$, respectively. The uncertainties in fixing these axes are embedded in our overall error bars (see Fig. 2), as we do not implement the unitary $U_{\|}(\hat{q})$ separately. Indeed, this unitary is immersed in the QHQ configuration that implements the complete transformation of our array.

Now, because the experimentally determined geometric phase requires measuring maximal and minimal intensities, its value could turn inaccurate for those points in the evolution where $I_{\max} \approx (1 + r)/2$ or $I_{\min} \approx (1 - r)/2$ [see Eqs. (30) and (31)]. This situation arose, for instance, for the first five points of Fig. 2(a). Occasionally, imaginary values were obtained, accompanied by large error bars. In such cases we made use of the relationship linking Φ_g to the solid angle enclosed by the state's trajectory on the Poincaré sphere [see Eq. (18)]. In the case of Fig. 2(a), we obtained Φ_g by performing a complementary evolution in the following sense. The targeted path was part of a circle and had an initial point A and a final point B (see Fig. 4). This open path can be closed in two ways. The first is by completing the circular path so that A is its initial and final point. Such a closed path subtends a solid angle Ω. A second closed path is obtained by joining A and B with a great circle (see Fig. 4). Such a closed path subtends a solid angle Ω_2, which determines Φ_g. Thus, Ω becomes the sum of two solid angles, one corresponding to the targeted phase, Ω_2, and a complementary one, Ω_1. Both Ω and Ω_1 could be accurately determined by measuring their corresponding geometric phases. Thus, $\Omega_2 = \Omega - \Omega_1$, viz., Φ_g, could be accurately determined as well. There are, however, exceptional cases in which the geometric phase cannot be accurately measured by means of the present method. In the case of Fig. 2(b), for instance, Φ_g has a large gradient in the region between $\alpha = 75^\circ$ and $\alpha = 100^\circ$, where no reliable measurement outcomes could be obtained. Whether this is a method-independent feature is an issue that remains to be explored. Finally, in the case of Fig. 2(c), the values obtained by applying the general procedure showed large variances for the first points (small α). In order to get reliable values of Φ_g, we traversed the same curve twice and then subtracted the contribution to Φ_g that came from the first loop. This procedure proved to be robust against inaccuracies in data recording.

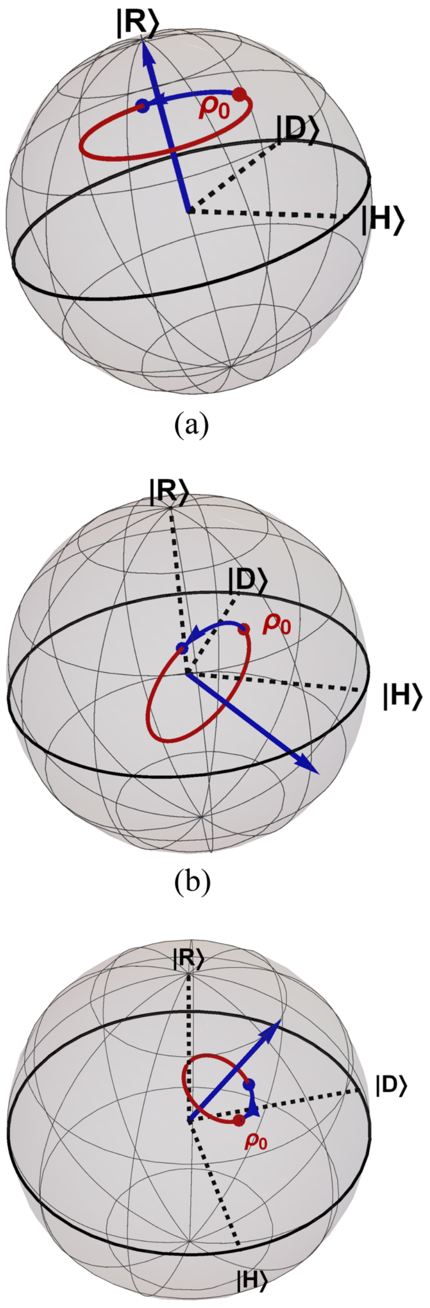

(a)

(b)

(c)

FIG. 3. Curves followed by the state in the Poincaré sphere as it evolves under the action of $U(\alpha)$. $|H\rangle$, $|D\rangle$, and $|R\rangle$ stand for horizontal, diagonal, and right-handed circular polarization, respectively. (a) Axis of rotation: $\hat{q} = (0,1,1)$. (b) Axis of rotation: $\hat{q} = (0.85, -0.45, -0.26)$. (c) Axis of rotation: $\hat{q} = (0.31, 0.4, 0.86)$.

Generally, there were several sources of experimental error. Reflection imperfections in the preparation stage of the array, due to nonideal BS, PBS, and mirrors, affect the degree of polarization of the input state. To circumvent this problem, we adjusted the first half-wave plate to compensate imbalances, while through quantum state tomography we made sure that the generated state was the targeted one. Furthermore, the angles of

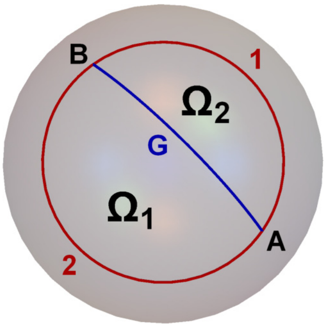

FIG. 4. The geometric phase acquired while following path A1B is directly related to solid angle Ω_2. This solid angle can also be found as the total solid angle enclosed by path A2B1A minus Ω_1. These solid angles determine the geometric phase accumulated along paths A2B1A and A2B, respectively. Path AGB is a geodesic (great circle) that closes the open curves A1B and A2B.

the wave plates could be set to within ±1°, causing cumulative errors. Thus, possible mismatches between targeted and actual values of the angles contributed to the error bars shown in Fig. 2. We should notice, however, that our method provides accurate values for Φ_g, even though this quantity may vary within quite different ranges. In Fig. 2(b), for example, Φ_g varies in a range that is roughly five times larger than that of Fig. 2(a) and roughly 20 times larger than that of Fig. 2(c).

IV. CONCLUSIONS

Our all-optical, polarimetric setup proved to be a useful tool to generate and test mixed-state geometric phases with great versatility. We were able to produce any desired mixed state and to generate Sjöqvist's geometric phase by submitting the state to unitary evolution along nongeodesic paths. Even though we restricted ourselves to the subset of circular trajectories in Poincaré space, any piecewise unitary evolution can be investigated with the same array. It should also be possible to generate geometric phases arising from nonunitary evolutions by using similar tools based on a polarimetric setup, but a somewhat more involved array is then required. Such an array is within reach for all-optical setups of the kind that we have exhibited here. Our all-optical setting has obvious advantages compared to neutron polarimetric and interferometric arrays [9,14,26–29] because it requires less demanding experimental resources and gives access to, in principle, arbitrary paths on the Poincaré sphere. This feature is particularly important in relation to possible simulations of noisy evolutions [30] that can be designed to test the robustness of geometric phases against decohering effects [13].

ACKNOWLEDGMENTS

This work was partially financed by DGI-PUCP (Grant No. 2015-224). D.B. and R.C. received financial support from CONCYTEC/FONDECYT.

[1] M. Ericsson, A. K. Pati, E. Sjöqvist, J. Brännlund, and D. K. L. Oi, Phys. Rev. Lett. **91**, 090405 (2003).
[2] D. M. Tong, E. Sjöqvist, L. C. Kwek, and C. H. Oh, Phys. Rev. Lett. **93**, 080405 (2004).
[3] O. Andersson and H. Heydai, Phys. Scr. **T163**, 014027 (2014).
[4] O. Viyuela, A. Rivas, and M. A. Martin-Delgado, Phys. Rev. Lett. **112**, 130401 (2014).
[5] J. Lages, R. Giust, and J.-M. Vigoureux, Phys. E (Amsterdam, Neth.) **59**, 6 (2014).
[6] O. Viyuela, A. Rivas, and M. A. Martin-Delgado, 2D Mater. **2**, 034006 (2015).
[7] A. Uhlmann, Rep. Math. Phys. **24**, 229 (1986).
[8] E. Sjöqvist, A. K. Pati, A. Ekert, J. S. Anandan, M. Ericsson, D. K. L. Oi, and V. Vedral, Phys. Rev. Lett. **85**, 2845 (2000).
[9] J. Klepp, S. Sponar, S. Filipp, M. Lettner, G. Badurek, and Y. Hasegawa, Phys. Rev. Lett. **101**, 150404 (2008).
[10] J. Du, P. Zou, M. Shi, L. C. Kwek, J.-W. Pan, C. H. Oh, A. Ekert, D. K. L. Oi, and M. Ericsson, Phys. Rev. Lett. **91**, 100403 (2003).
[11] J. Zhu, M. Shi, V. Vedral, X. Peng, D. Suter, and J. Du, Europhys. Lett. **94**, 20007 (2011).
[12] A. G. Wagh and V. C. Rakhecha, Phys. Lett. A **197**, 112 (1995).
[13] E. Sjöqvist, Physics **1**, 35 (2008).
[14] S. Filipp, J. Klepp, Y. Hasegawa, C. Plonka-Spehr, U. Schmidt, P. Geltenbort, and H. Rauch, Phys. Rev. Lett. **102**, 030404 (2009).
[15] G. Feng, G. Xu, and G. Long, Phys. Rev. Lett. **110**, 190501 (2013).
[16] D. Barberena, G. Gatti, and F. De Zela, J. Opt. Soc. Am. A **32**, 697 (2015).
[17] M. Ericsson, D. Achilles, J. T. Barreiro, D. Branning, N. A. Peters, and P. G. Kwiat, Phys. Rev. Lett. **94**, 050401 (2005).
[18] O. Ortíz, Y. Yugra, A. Rosario, J. C. Sihuincha, J. C. Loredo, M. V. Andrés, and F. De Zela, Phys. Rev. A **89**, 012124 (2014).
[19] S. Pancharatnam, Proc. Indian Acad. Sci. A **44**, 247 (1956); Reprinted in *Collected Works* of S. Pancharatnam (Oxford University Press, Oxford, 1975).
[20] J. Audretsch, *Entangled Systems: New Directions in Quantum Physics* (Wiley-VCH, Chichester, UK, 2007).
[21] N. Mukunda and R. Simon, Ann. Phys. (NY) **228**, 205 (1993).
[22] R. Simon and N. Mukunda, J. Phys. A **25**, 6135 (1992).
[23] P. G. Kwiat and R. Y. Chiao, Phys. Rev. Lett. **66**, 588 (1991).
[24] J. J. Thorn, M. S. Neel, V. W. Donato, G. S. Bergreen, R. E. Davies, and M. Beck, Am. J. Phys. **72**, 1210 (2004).
[25] P. Grangier, G. Roger, and A. Aspect, Europhys. Lett. **1**, 173 (1986).
[26] J. Klepp, S. Sponar, Y. Hasegawa, E. Jericha, and G. Badurek, Phys. Lett. A **342**, 48 (2005).
[27] R. A. Bertlmann, K. Durstberger, Y. Hasegawa, and B. C. Hiesmayr, Phys. Rev. A **69**, 032112 (2004).
[28] S. Werner, Found. Phys. **42**, 122 (2012).
[29] S. Sponar, J. Klepp, K. Durstberger-Rennhofer, C. Schmitzer, H. Bartosik, H. Geppert, M. Both, G. Badurek, and Y. Hasegawa, New J. Phys. **14**, 053032 (2012).
[30] S. P. Walborn, C. H. Monken, S. Pádua, and P. H. Souto Ribeiro, Phys. Rep. **495**, 87 (2010).